

Endoscope-tip interferometer for ultrahigh resolution frequency domain optical coherence tomography in mouse colon

Alexandre R. Tumlinson

Center of Biomedical Engineering and Physics, Medical University of Vienna, Vienna, Austria
Division of Biomedical Engineering, The University of Arizona, Tucson, Arizona, USA

Jennifer K. Barton

Division of Biomedical Engineering, The University of Arizona, Tucson, Arizona, USA

Boris Považay, Harald Sattman, Angelika Unterhuber, Rainer A. Leitgeb,
Wolfgang Drexler

Center of Biomedical Engineering and Physics, Christian Doppler Laboratory, Medical University of Vienna,
Vienna, Austria

wolfgang.drexler@meduniwien.ac.at

Abstract: Frequency domain optical coherence tomography (FD-OCT) allows interferometer topologies with simplified system construction and handling. Problems of dispersion and polarization matching between the sample and reference arms, as well as beamsplitter spectral non-uniformity, are mitigated when the interferometer is wholly contained in the endoscope tip. A common path set-up, using a reference reflection originating from the inside surface of the glass envelope at the distal end of the endoscope, and an alternative approach with more efficient collection of the reference light using a novel beamsplitter design have been developed. High-speed (20,000 A-lines/s) ultrahigh axial resolution (2.4 μm) tomograms of mouse colon have been acquired using a 2 mm outer diameter endoscope *in vivo*. The FD-OCT system uses a compact mode-locked Ti:Al₂O₃ laser emitting a broad spectrum (160 nm full-width-half-maximum) centered at 800 nm in combination with a CCD based, spectrally sensitive detector.

©2006 Optical Society of America

OCIS codes: (170.4500) Optical coherence tomography; (170.2150) Endoscopic imaging; (120.3890) medical optics instrumentation.

References and links

1. F. I. Feldchtein, J. Bush, G. Gelikonov, V. Gelikonov, and S. Piyevsky, "Cost effective, all-fiber autocorrelator based 1300 nm OCT system," in *Coherence domain optical methods and optical coherence tomography in biomedicine IX*, V.V. Tuchin, J.A. Izatt, J.G. Fujimoto, eds., Proc. SPIE **5690**, 349-355 (2005).
2. H. D. Ford, R. Beddows, P. Casaubieilh, and R. P. Tatum, "Comparative signal-to-noise analysis of fibre-optic based optical coherence tomography systems," *J. Mod. Opt.* **52**, 1965-1979 (2005)
3. A. F. Fercher, C. K. Hitzenberger, M. Sticker, R. Zawadzki, B. Karamata, and T. Lasser, "Numerical dispersion compensation for partial coherence interferometry and optical coherence tomography," *Opt. Express* **9**, (2001), <http://www.opticsexpress.org/abstract.cfm?URI=OPEX-9-12-610>
4. J. F. de Boer, C. E. Saxer, and J. S. Nelson, "Stable carrier generation and phase-resolved digital data processing in optical coherence tomography," *Appl. Opt.* **40**, 5787-5790 (2001).
5. M. Wojtkowski, V. J. Srinivasan, T. H. Ko, J. G. Fujimoto, A. J. Kowalczyk, and J.S. Duker, "Ultrahigh-resolution, high-speed, Fourier domain optical coherence tomography and methods for dispersion compensation," *Opt. Express* **12**, 2404-2422 (2004), <http://www.opticsexpress.org/abstract.cfm?URI=OPEX-12-11-2404>
6. A. F. Fercher, C. K. Hitzenberger, G. Kamp, S. Y. El Zaiat, "Measurement of intraocular distances by backscattering spectral interferometry," *Opt. Commun.* **117**, 43-48 (1995).

7. T. Mitsui, "Dynamic range of Optical Reflectometry with Spectral Interferometry," *Jpn. J. Appl. Phys.* **38**, 6133-6137 (1999).
8. P. Andretzky, M. Knauer, F. Kiesewetter, and G. Haeusler, "Optical coherence tomography by spectral radar: improvement of signal-to-noise ratio," in *Coherence Domain Optical Methods in Biomedical Science and Clinical Applications IV*, V. V. Tuchin, J. A. Izatt, and J. G. Fujimoto, eds., *Proc. SPIE* **3915**, 55-59 (2000).
9. R. A. Leitgeb, C. K. Hitzenberger, and A. F. Fercher, "Performance of Fourier domain vs. time domain optical coherence tomography," *Opt. Express* **11**, 889-894 (2003), <http://www.opticsexpress.org/abstract.cfm?URI=OPEX-11-8-889>
10. M. A. Choma, M. V. Sarunic, C. Yang, and J. A. Izatt, "Sensitivity advantage of swept source and Fourier domain optical coherence tomography," *Opt. Express*, **11**, 2183 (2003), <http://www.opticsexpress.org/abstract.cfm?URI=OPEX-11-18-2183>
11. J. F. deBoer, B. Cense, B. H. Park, M. C. Pierce, G. J. Tearney, and B. E. Bouma, "Improved signal-to-noise ratio in spectral-domain compared with time-domain optical coherence tomography," *Opt. Lett.* **28**, 2067-2069 (2003).
12. R. A. Leitgeb, W. Drexler, A. Unterhuber, B. Hermann, T. Bajraszewski, T. Le, A. Stingl, and A. F. Fercher, "Ultrahigh resolution Fourier domain optical coherence tomography," *Opt. Express* **12**, 2156-2165 (2004), <http://www.opticsexpress.org/abstract.cfm?URI=OPEX-12-10-2156>
13. S. R. Chinn, E. A. Swanson, J. G. Fujimoto, "Optical coherence tomography using a frequency-tunable optical source," *Opt. Lett.* **22**, 340-341 (1997).
14. S. H. Yun, G. J. Tearney, J. F. deBoer, N. Ifimia, B. E. Bouma, "High-speed optical frequency-domain imaging," *Opt. Express* **11**, 2953-2963 (2003), <http://www.opticsexpress.org/abstract.cfm?URI=OPEX-11-22-2953>
15. Y. Yasuno, S. Makita, T. Endo, M. Itoh, T. Yatagai, M. Takahashi, C. Katada, and M. Mutoh, "Polarization-sensitive complex Fourier domain optical coherence tomography for jones matrix imaging of biological samples," *Appl. Phys. Lett.* **11**, 3023-3025 (2004).
16. B. Cense, N. A. Nassif, T. C. Chen, M. C. Pierce, S. H. Yun, B. H. Park, B. E. Bouma, G. J. Tearney, and J. F. deBoer, "Ultrahigh-resolution high-speed retinal imaging using spectral-domain optical coherence tomography," *Opt. Express* **12**, 2435-2447 (2004), <http://www.opticsexpress.org/abstract.cfm?URI=OPEX-12-11-2435>
17. S. H. Yun, G. J. Tearney, J. F. deBoer, and B. E. Bouma, "Pulsed-source and swept source spectral-domain optical coherence tomography with reduced motion artifacts," *Opt. Express* **12**, 5614-5624 (2004), <http://www.opticsexpress.org/abstract.cfm?URI=OPEX-12-23-5614>
18. A. B. Vakhtin, D. J. Kane, W. R. Wood, and K. A. Peterson, "Common-path interferometer for frequency-domain optical coherence tomography," *Appl. Opt.* **42**, 6953-6958 (2003).
19. P. Koch, G. Huettmann, D. Boller, J. Weltzel, and E. Koch, "Ultra high resolution FDOCT system for dermatology," in *Coherence domain optical methods and optical coherence tomography in biomedicine IX*, V. V. Tuchin, J. A. Izatt, and J. G. Fujimoto, eds., *Proc. SPIE* **5690**, 24-30 (2005).
20. J.K. Barton, D.B. Dal-Ponte, S.K. Williams, B. Ford, and M.R. Descour, "Imaging vascular implants with optical coherence tomography," in *Coherence domain optical methods and optical coherence tomography in biomedicine IV*, V.V. Tuchin, J.A. Izatt, J.G. Fujimoto, eds., *Proc. SPIE* **3915**, 229-236 (2000).
21. P.R. Herz, Y. Chen, A.D. Aguirre, and J.G. Fujimoto, "Ultrahigh resolution optical biopsy with endoscopic optical coherence tomography," *Opt. Express* **12**, 3532-3542 (2004), <http://www.opticsexpress.org/abstract.cfm?URI=OPEX-12-15-3532>
22. J. A. Izatt, M. V. Sivak, A. M. Rollins, A. Hiroii, T. Hirata, and S. Lizuka "Optical imaging device," United States Patent 6,564,089 (13 May 2003).
23. A. R. Tumlinson, J. K. Barton, J. McNally, A. Unterhuber, B. Hermann, H. Sattman, and W. Drexler, "An achromatized endoscope for ultrahigh-resolution optical coherence tomography," in *Optical Coherence Tomography and Coherence Techniques II*, W. Drexler, ed., *Proc SPIE* **5861**, 586110 (2005).
24. U. Sharma, N. M. Fried, and J. U. Kang, "All-fiber common-path optical coherence tomography: sensitivity optimization and system analysis," *IEEE J. Sel. Top. Quantum Electronics.* **11**, 799-805 (2005).
25. R. A. Leitgeb, C. K. Hitzenberger, A. F. Fercher, and T. Bajraszewski, "Phase-shifting algorithm to achieve high-speed long-depth-range probing by frequency-domain optical coherence tomography," *Opt. Lett.* **28**, 2201-2201 (2003).
26. M. A. Choma, C. Yang, and J. A. Izatt, "Instantaneous quadrature low-coherence interferometry with 3*3 fiber-optic couplers," *Opt. Lett.* **28**, 2162-2164 (2003).
27. J. Zhang, J. S. Nelson, and Z. Chen, "Removal of a mirror image and enhancement of the signal-to-noise ratio in Fourier-domain optical coherence tomography using an electro-optic phase modulator," *Opt. Lett.* **30**, 147-149 (2005).
28. M. A. Choma, A. K. Ellerbee, C. Yang, A. L. Creazzo, and J. A. Izatt, "Spectral-domain phase microscopy," *Opt. Lett.* **30**, 1162-1164 (2005).
29. A. Szkulmowska, M. Wojtkowski, I. Gorczynska, T. Bajraszewski, P. Targowski, and A. Kowalczyk, "Coherent noise-free ophthalmic imaging by spectral optical coherence tomography," *J. Phys. D: Appl. Phys.* **38**, 2606-2611 (2005).
30. M. V. Sivak Jr, K. Kobayashi, J. A. Izatt, A. M. Rollins, R. Ung-Runyawee, A. Chak, R. C. Wong, G. A. Isenberg, and J. Willis, "High-resolution endoscopic imaging of the GI tract using optical coherence tomography," *Gastrointest. Endosc.* **51**, 474-479 (2000).

31. T. Hillman and D. Sampson, "The effect of water dispersion and absorption on axial resolution in ultrahigh-resolution optical coherence tomography," *Opt. Express* **13**, 1860-1874 (2005)
<http://www.opticsexpress.org/abstract.cfm?URI=OPEX-13-6-1860>
 32. P. B. Boivin, K. Washington, K. Yang, J. M. Ward, T. P. Pretlow, R. Russel, D. G. Besselson, V. L. Godfrey, T. Doetschman, W. F. Dove, H. C. Pitot, R. B. Halberg, S. H. Itzkowitz, J. Groden, and R. J. Coffey, "Pathology of mouse models of intestinal cancer: consensus report and recommendations," *Gastroenterology* **124**, 762-777 (2003).
-

1. Introduction

Widespread clinical application of optical coherence tomography (OCT) endoscopy requires that probes be quickly replaceable by hospital staff. Since uncompensated inter-endoscope pathlength differences of less than 1 mm adversely affect performance of conventional Michelson interferometer-based OCT devices, designs insensitive to minor variations in the endoscopes geometry are desirable. Progress towards this goal is demonstrated by Imalux Corporation's recent United States Food and Drug Administration cleared endoscopic system that uses a topology including a fiber stretching autocorrelator with Faraday mirrors to enable interchange of probes without a predefined probe length or compensation for a standard resolution application [1, 2]. Ultrahigh axial resolution OCT (UHR-OCT) presents a special challenge because dispersion and polarization matching between arms of the interferometer must be performed over a wide bandwidth that may be centered far away from the zero dispersion point of the materials used. Numerical methods for compensating dispersion are computationally expensive, sensitive to noise, and perform best when the real dispersion mismatch is already well compensated in the system [3-5].

Frequency domain OCT (FD-OCT) simultaneously provides a signal-to-noise (SNR) advantage over the traditional time domain method (TD-OCT) and requires no moving parts in the reference arm [6-12]. This combination allows imaging at rates more than an order of magnitude higher than in TD-OCT and is responsible for rapid development of this branch of OCT [13-16]. Faster imaging with FD-OCT enabled Yun *et al.* to take endoscopic tomograms with reduced motion artifacts [17]. Vakhtin *et al.* showed, in a freespace interferometer, that the static reference arm also allows a "common path" approach where the reference reflection comes from a surface within the sample arm rather than in a physically separated reference arm. In this example, the back reflection from the proximal surface of a thin glass slide in contact with the sample was used as the reference. They noted much improved ease of alignment and imaging stability [18]. Koch *et al.* demonstrated a system that used fiber to couple the source and detector to a handheld probe containing a free space interferometer to reduce sensitivity to system vibration and fiber induced polarization and dispersion mismatch [19].

Backreflections occurring at the inner surface of the endoscope window element are usually considered a nuisance to be suppressed. Coating window surfaces [20], inserting index matching fluid [21], or using an off-normal beam exit angle [22, 23] express a variety of solutions to this problem.

We explore the use of both common path and Michelson interferometer topologies integrated into the distal tip of small diameter endoscopes with FD-OCT. Our common path arrangement uses the backreflection from the inner surface of the endoscope window as a reference. This simple arrangement demonstrates the advantages of a distally integrated interferometer for endoscopic FD-OCT, but also highlights the sensitivity and artifact problems of using a window surface to provide the reference reflection. Our Michelson arrangement maintains the advantages of having no flexible fiber in the difference path of the interferometer but performs with higher efficiency and theoretically superior dispersion characteristics. Finally we demonstrate the Michelson based endoscope to collect ultrahigh axial resolution tomograms of mouse colon *in vivo*.

2. Methods

2.1. FD-OCT endoscope with common path interferometer

The setup for the common path endoscopic system is shown in Fig. 1. The light source is a compact femtosecond pulsed Ti:Al₂O₃ laser with 160 nm bandwidth at full-width-half-maximum (FWHM) centered at 800 nm (Femtosource Integral OCT, Femtolasers Produktions GmbH) enabling a theoretical axial resolution of 1.8 μm in tissue. A 90/10 fiber beamsplitter is used to couple 10% of the source light into the endoscope and 90% of the light from the endoscope (and thereby from the sample) back to the detector. Note that this beamsplitter does not contribute to the difference path in an interferometer (and would optimally be replaced by an optical circulator). Light in the endoscope is focused by a 1 mm diameter, 0.33 pitch, gradient index lens and redirected by an air-spaced mirror through a 100 μm thick fused silica window to a 10 μm diameter spot located 300 μm deep in the tissue. The cylindrically curved inner surface of the uncoated window acts as a beamsplitter of a common path interferometer. A water-based lubricant is used for index matching at the window-skin interface to decrease this reflection. Therefore, the dominant reference reflection comes from the inside surface of the window. The interference signal returning from the endoscope passes a polarization controller to optimize transmission efficiency at the reflective diffraction grating inside the spectrometer. The spectrometer comprises: a transmissive 150 mm focal length collimator, a 600 g/mm reflective grating, a transmissive F/2, 150 mm focal length objective, and a high speed linear CCD array. The 2 kpixel CCD array has 12-bit dynamic range with a maximum readout of 20,000 lines per second. CCD receiver noise and full well capacity are 90 and 1.8E5 electrons respectively. Detector quantum efficiency is 0.6 at 800 nm. The resolution of the CCD allows calculation to an optical depth of 1.4 mm, however limited spectrometer resolution and finite pixel size (14 μm) causes a finite spectral linewidth to be measured at each pixel and thereby reduces usable depth range to less than 1 mm. Lateral scanning was performed at 14 mm/s corresponding to a sampling density of 1400 axial-scans/mm. The 2 mm outer diameter endoscope pushes and pulls the tip optics via mechanical linkage to an external stepper motor driven linear actuator. Tomograms are recorded from *in vivo* normal human fingertip skin at 3 mW incident power.

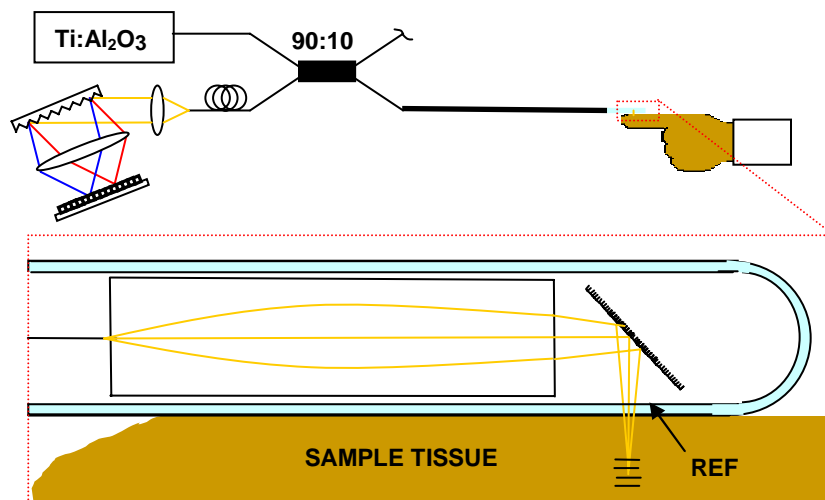


Fig. 1. Experimental setup utilizing common path interferometer topology. Spatially encoded FD-OCT is achieved using a broad bandwidth Ti:Al₂O₃ laser and a diffraction grating based spectrometer yielding 2.9 μm axial resolution at 20,000 A-lines/s. The reference reflection originates at the inside surface (REF) of the endoscope window, and is separated by the window thickness (100 μm) from the tissue.

System performance is quantified by examining resulting tomograms. Axial resolution is measured from the specular reflection originating from the outer surface of the window. The dynamic range is calculated from the maximum valued voxel in each axial-scan, excluding the top 200 voxels which contain the specular reflections from the outer window-skin interfaces, and comparing that to the standard deviation of the noise in an area near the bottom of the image. Image shown is first converted to logarithmic intensity scale, and then smoothed by convolution with a Gaussian kernel with FWHM = 2 pixels to reduce speckle contrast.

2.2. FD-OCT endoscope with distally integrated Michelson interferometer

The endoscope tip of the above OCT system is replaced with a novel distally integrated micro beamsplitter shown in Fig. 2. A 1 mm diameter, 0.33 pitch gradient index lens focuses probe beam. A metal hybrid non-polarizing beamsplitter surface located 1.2 mm downstream receives the converging cone of light, reflects 80% into the sample arm, transmits 10% to the reference arm, and absorbs about 10% of the incident light. The aluminum coated reference mirror lies 0.8 mm beyond the splitter in order to place the reference 100 μm in optical path length proximal to the outer envelope surface. The reference mirror's 0.83 mm radius of curvature matches the incident wavefront for maximum coupling efficiency of the return beam. The 49 degree beamsplitter angle sends the output beam off normal to suppress coupling of backreflections from the exit surface of the beamsplitter and the envelope window, which could cause spurious references. The distance from the axial centerline for the prism to the flat output surface is 0.4 mm. The difference in material path length from the solid thickness of BK7 in the reference arm and the airgap in the sample arm corrects for second order dispersion of water to a depth of 200 μm . The output beam comes to a 10 μm diameter focused spot 300 μm beyond the outside surface of the endoscope.

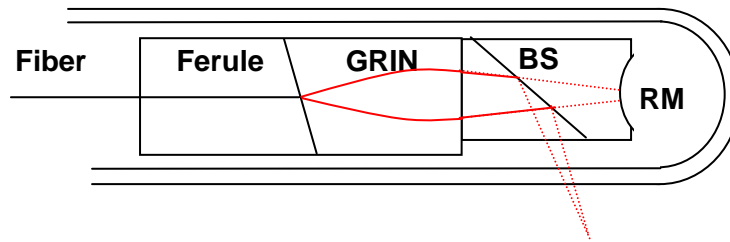


Fig. 2. The distally integrated micro beamsplitter allows improved backreflection and re-coupling from the reference arm. The combined beam path is shown in solid red while sample and reference paths are indicated by dashed lines. The beam splitter (BS) and reference mirror (RM) are indicated.

The choice of beamsplitter ratio is supported by a theoretical sensitivity [9] and dynamic range [12] calculation. The power returning from the reference arm is the source power ($P_o=0.8$ mW) multiplied by the square of the beamsplitter transmission (γ_r) and the assumed reflectivity and coupling efficiency of the reference reflection back into the fiber ($R_r=0.7$). The power returning from the sample arm is the source power multiplied by the square of the beamsplitter reflection (γ_s) and the assumed reflectivity and coupling efficiency of the sample ($R_s=-40\text{dB}$). No incoherent light returns from either arm. When calculating beamsplitter reflection and transmission a constant loss of 10% was assumed. The spectrometer efficiency ($\rho=0.19$) was assumed as well as the degree of polarization ($\Pi=1$). The number of detector elements ($N=2048$), quantum efficiency ($\eta=0.6$), exposure time ($\tau=50$ μs), center frequency ($\nu_o=3.75\text{E}14$ Hz), effective line width ($\Delta\nu_{\text{eff}}=7.57\text{E}13$ Hz), CCD receiver noise ($\sigma_{\text{rec}}=90$ electrons) and full well capacity of a CCD element ($N_{\text{sat}}=1.8\text{E}5$ electrons) can be determined from the specification of the rest of the system. The fill fraction of the well capacity due to the reference (γ) is calculated from the power returning from the reference arm as defined above.

Results (shown in Fig. 3.) of the simulation indicate that high sensitivity (100 dB) and dynamic range (68 dB) can be achieved at our chosen beamsplitter ratio.

2.3. Imaging mouse colon *in vivo*

Normal mice, approximately ten weeks old, were examined *in vivo*. Mice were anesthetized with a mix of Ketamine – Xylazine delivered with an intraperitoneal injection. The endoscope was coated with a water based lubricant and inserted in the anus to a depth of 33 mm. Longitudinal cross-sections were obtained at 2 mm/s with less than 1 mW power incident on the sample. Image shown is first converted to logarithmic intensity scale, resampled horizontally (6:1) to achieve isotropic spatial scale, and then smoothed by convolution with a Gaussian kernel with FWHM = 2 pixels to reduce speckle contrast. Protocols were approved by the Medical University of Vienna Institutional Animal Care and Use Committee. System performance was quantified as described for the common path configuration above.

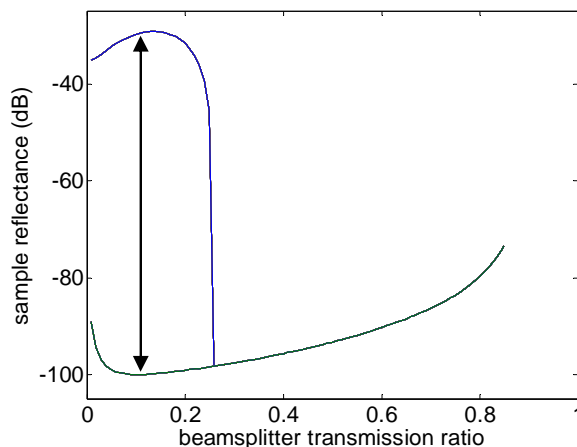


Fig. 3. Theoretical sensitivity and dynamic range vs. beamsplitter transmission ratio in the Michelson arrangement. The lower line (green) indicates the sample reflectance that yields a signal to noise ratio of unity (max sensitivity = -100 dB), while the upper line (blue) indicates the largest sample reflectance that will not saturate the detector. The difference between the two lines is the dynamic range (68 dB) indicated by the arrow at the chosen beamsplitter ratio (0.1). The detector is saturated for beamsplitter transmission greater than 0.26.

3. Results

3.1. Using the common path approach

An *in vivo* tomogram of the palmar surface of a human fingertip (Fig. 4.) shows that high axial resolution (corresponding to $2.9 \mu\text{m}$ FWHM in tissue with index = 1.4) has been achieved with no additional effort to match pathlength, dispersion, or polarization between sample and reference arms. The tomogram exhibits an average dynamic range of 27 dB. The tomogram is displayed with dimensions corrected for an average refractive index of 1.4 in tissue. Sweat ducts are clearly resolved in the stratum corneum, and penetration reaches slightly into the stratum spinosum, approximately 0.4 mm into the tissue. The reflection from the outer surface of the endoscope window is observed as a thin line, frequently in contact with tissue, $145 \mu\text{m}$ in optical thickness from the top of the image. The outer surface of the window, which lies relatively close to the beam focus, would present a stronger back reflection than the inside surface, but it does not because of efficient index matching by the lubricant. A faint double image displaced $\sim 100 \mu\text{m}$, or $145 \mu\text{m}$ in optical thickness, vertically is the result of this second “reference” reflection coming from the outer surface of the endoscope window. This double image is noticeable at the top of the image space “inside” the window. Double image artifacts are mild in the fingertip image but result in unacceptably

poor image quality in mouse colon (not shown), due to less effective index matching at the outer surface and increased brightness of superficial tissue layers.

3.2 With the distally integrated Michelson interferometer

An *in vivo* tomogram of the luminal surface of a normal mouse colon (Fig. 5.) indicates similarly high axial resolution ($2.4\ \mu\text{m}$ FWHM in tissue with index = 1.4) has been achieved with a fixed, distally integrated reference arm completely contained in the tip of the endoscope. The tomogram exhibits an average dynamic range of 33 dB. The tomogram is displayed with dimensions corrected for an average tissue index of 1.4. The colonic mucosa appears as a thick, moderately to strongly scattering region at the top of the image. Nearly vertical, less scattering bands within mucosa correspond to glandular crypts. A light horizontal band at the tissue surface corresponds well with the aligned cells of the luminal epithelium. Boundaries of the muscularis mucosa and submucosa appear as bright, thin lines of highly scattering tissue. The signal penetrates the full thickness of the moderately scattering muscularis externa, allowing visualization of surrounding serosa (or adventitia when the colon is connected to surrounding tissues.) The parasitic reflection from the outer surface of the endoscope window is almost completely suppressed by the off axis output angle. This image is free from double image artifacts seen in the common path image.

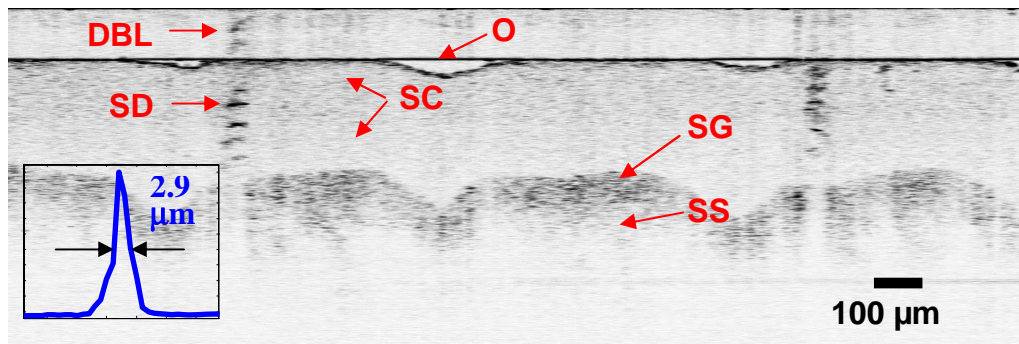


Fig. 4. Common path endoscopic UHR FD-OCT tomogram of human fingertip skin exhibits high stability and axial resolution ($2.9\ \mu\text{m}$). Image features include: stratum corneum (SC), stratum granulosum (SG), stratum spinosum (SS), sweat duct (SD), the outer surface of endoscope window (O), and a faint double image (DBL) of stratum corneum using endoscope window outer surface as a reference. Inset graph shows axial point spread function detail.

4. Discussion

An interferometer integrated into the distal tip of the endoscope overcomes some of the most troublesome aspects of UHR-OCT endoscopy. This geometry removes the need for a separate adjustable reference arm and therefore reduces system complexity and cost. Reference compensation is not required when a new endoscope is attached to the system, allowing “plug-and-play” utility that facilitates widespread clinical application, without the need for costly tolerances on the length of the endoscope fiber. The dynamically changing dispersion and polarization mismatch between sample and reference reflections introduced by fiber in the difference path of interferometer is eliminated by design, allowing systems to achieve good, and potentially better and more stable, resolution and sensitivity without dispersion compensating prisms and polarization paddles. The beamsplitters demonstrated in both arrangements are spectrally flat over a much wider range than the fiber beamsplitters that are currently used in traditional Michelson interferometers. The spectral flatness of both configurations is currently limited by the chromatic error in the focusing lens and the extent to which the reference is reflected into the fiber’s spectrally dependant numerical aperture. The cost of placing the beamsplitter in the endoscope tip is inaccessibility after manufacture[24]. Optimization of the reference reflection strength occurs as part of the design process rather than as part of an experimental procedure. Similarly, it would be very challenging to

implement modulation of the reference arm delay to resolve the +/- spatial frequency ambiguity caused by Fourier transform of a real valued spectrum [25-27].

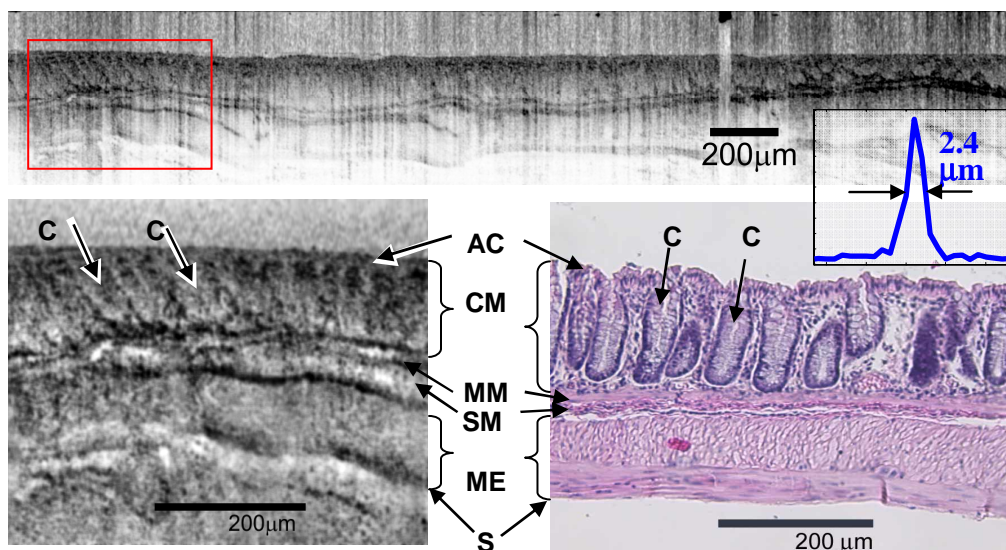


Fig. 5. Endoscopic UHR-OCT (reflectivity) tomogram (above) versus stained histologic (absorptive) crosssection (lower right) of *in vivo* mouse colon with distally integrated beam splitter enables visualization of colonic mucosa (CM), muscular mucosa (MM), submucosa (SM), muscularis externa (ME), and serosa (S) layers. Contrast enhanced portion, using local histogram equalization (lower left) shows a surface layer of apical crypt cells (AC) as well as vertical structures in the mucosa that may correspond to crypt boundaries (C). Corresponding structures are marked in the age and strain matched histology image. Inset graph shows axial point spread function detail.

The common path interferometer using a reflection from the endoscope window as a reference is an extremely simple self-referenced solution. The image position is stable relative to the window even if the mechanical tolerances of the endoscope allow the separation between the tip optics and protective envelope to vary. This stability improves image quality and may enable sensitive phase measurement [28]. Unfortunately, inefficient collection of the reference reflection results in low signal to noise and significant artifacts. This poor reference coupling is due to the mismatch in curvature between the beam wavefront and the envelope surface. Efficiency of reference coupling in this configuration depends on distance between the tip optics and the window, attitude of the tip optics relative to the window, and condition of the window as a reflecting or scattering surface. Since all of these factors may change over the course of a linear scan or rotation of the device, the coupling efficiency of the reference and thus the SNR may vary with transverse scanning. Best sensitivity is reached in OCT when the interference term between the sample and reference is maximized to fill as much of the dynamic range of the detector as possible. In spatially resolved FD-OCT practice with biological samples, which have inherently low backscattering, one first attempts to get as much light back from the sample as can be achieved, given the irradiation limits of the tissue and available source power. Then the strength of the reference signal is maximized to fill the remaining dynamic range of the detector. The optimized reference power will commonly be much stronger than the power returning from the sample. A single strong reference reflection improves the signal strength relative to the internal crosscorrelation signals as well as ghost reflections resulting from spurious “references” [9]. At first glance, one expects that the reflection of the window can be enhanced by adding a specifically highly reflecting (or backscattering) surface that will dominate over other weaker reflections. There are two significant problems with this solution that result in higher losses and lower SNR. First, the coupling efficiency of the reflected wave is poor because the wavefront curvature does not

match the shape of the window well. Lens design simulations predict that only one to two percent of the light reflected from the window is coupled back in to the fiber. To achieve a strong reference signal, a highly reflective coating would be required and the interferometer would be inefficient in its collection of the sample beam. Second, if the reflection from one of the window surfaces is used as a reference, the reflection from the nearly parallel opposite surface of the window must be well suppressed in order to avoid a spurious reference. For example, a nearly four percent reflection from an uncoated inner surface would be significant in comparison to even a very highly reflective coating on the outside surface.

We have chosen to increase the strength of the reference reflection by introducing a separate beam path using a prism beamsplitter after the focusing lens. This distally integrated Michelson interferometer shares many of the advantages of the common path topology by eliminating the fiber in the difference path, which is generally responsible for dispersion and polarization mismatch in endoscopic OCT. The wavefront-matched radius on the reference mirror allows efficient collection of the reflected beam and more than compensates for losses associated with the uncollected return channel in a Michelson setup. Additionally, because the reference path is a small monolithic block, the geometry and the strength of the reference coupling in this configuration do not vary with transverse scanning. Changing the reflectivity of the beamsplitter potentially allows any ratio of sample to reference power. The final optimization of beamsplitter reflectivity depends on the source power available, the power that the sample can tolerate, the efficiency of the entire system, noise and dynamic range of the spectrometer, and the imaging speed desired. In the end, source attenuation, detector gain and imaging speed may be used as compensators to optimize system sensitivity after endoscope construction. In our case, the sensitivity achieved appears to fall short of the theoretical prediction. A likely source of error in this prediction is the assumption of zero incoherent light incident on the detector. Incoherent light backreflected from imperfect fiber couplings or interfaces within the endoscope fill the dynamic range of the detector and add noise but do not contribute to the signal. It is also likely that coupling from the reference arm, although greatly improved by the wavefront curvature matched reference mirror, was not as good as assumed in the simulation. Autocorrelation artifact also significantly degrades image quality, particularly at the top of the image, where the signal from the tissue is fortunately strong. Szkulmowska *et al.* have shown that autocorrelation artifact can be maintained below the noise floor while maintaining useful sensitivity and dynamic range by controlling the source power and appropriately attenuating the reference arm [29]. We believe that with further optimization and improved construction, this endoscope geometry should allow sensitivity that is as good as is achieved by FD-OCT endoscopes with a separate, fiber-based, reference arm. Changing the axial length of the reference arm portion of the beamsplitter prism allows the reference to be placed at any depth, including beyond the endoscope window when a positive working distance is desired [30]. The prism beamsplitter also allows flexibility to modify the dispersion of the reference arm to compensate for water dispersion a short distance into the tissue. This arrangement also permits the use of an intentionally off-normal beam exit angle to suppress unwanted backreflections as an alternative to coatings or index matching.

Dispersion and absorption by the sample, recently theoretically reviewed by Hillman and Sampson[31], play an important role in broadening the realized axial point spread function beyond the ideal resolution predicted by the source bandwidth alone. The endoscopes demonstrated in the current work remove the major source of endoscopic system induced dispersion mismatch by removing the long sections of coiled and moving fiber from the difference path of the interferometer. Dispersion of the tissue remains a problem and will degrade imaging performance as the axial imaging distance varies from the point of best dispersion match. In the case of the common path endoscope, the zero delay is identical to the position of best dispersion match. Therefore, the dispersion of the glass window is additive to the dispersion of the tissue and best axial resolution is predicted at the surface of the tissue, and will degrade with further depth into the tissue. In the case of the Michelson arrangement, one can design such that the point of best second order dispersion match lies some distance

into the tissue (modeled as water) – even though the zero delay lies within the endoscope. In our case best axial resolution is designed for a distance 200 μm into the tissue. This compensation method is expected to limit the maximum axial distance away from this best match point, minimize axial point spread broadening, and provide the best starting point for numerical post processing methods which might attempt to correct depth dependant dispersion effects.

High speed FD-OCT tomograms of mouse colon show features comparable to those seen in slow scanning ultra high resolution time domain tomograms of similar tissue [23], albeit with reduced penetration depth due to signal falloff at points far from the zero delay point. Most studies of mouse colon examine early neoplastic changes in the mucosa [32], which is only a few hundred microns thick, so it appears that spatially encoded FD-OCT is useful for this tissue. The increase in speed, and simultaneous increase in ease of use make this method very attractive for future studies characterizing this widely used animal model.

Acknowledgments

Support for this project includes support from the following sources: NIH(R01 CA109835, R24 CA83148), The University of Arizona Optics Initiative, FWF P14218-PSY, FWF Y 159-PAT, CRAF-1999-70549, ONB Jubiläumsfondprojekt Nr. 10506, the Christian Doppler Society, FEMTOLASERS GmbH, and the Fulbright Commission.